

Thermotropic Properties of Organic Nanocrystals Embedded in Ultrasmall Crystallization Chambers

Jeong-Myeong Ha, Marc A. Hillmyer, and Michael D. Ward*

The Department of Chemical Engineering and Materials Science and the Department of Chemistry, University of Minnesota, Minneapolis, Minnesota 55455

Received: October 4, 2004; In Final Form: November 10, 2004

Crystallization of organic compounds in nanometer-scale channels of controlled pore glass (CPG) and porous polystyrene (p-PS), the latter prepared by etching of the polylactide (PLA) component of shear-aligned PS–PLA diblock copolymers, produces crystals with dimensions that reflect the size constraints imposed by the channels. The nanoscopic dimensions of the organic crystals embedded in the channels result in a substantial melting point depression compared with the bulk, as demonstrated here for 2,2,3,3,4,4-hexafluoro-1,5-pentanediol (HFPD) and (*R*)-(+)-3-methyladipic acid (R-MAA). The melting points decreased with decreasing channel diameter, consistent with the increasing surface-area-to-volume ratio of the crystals. Furthermore, at these length scales the latent heat of melting decreased with decreasing crystal size. The melting point depression for both HFPD and R-MAA was greater in p-PS than in CPG, which can only be explained by interactions of the nanocrystals and their corresponding melts with the channel walls. Collectively, these discoveries reveal that simplified descriptions used in previous investigations of embedded crystals, which were limited to porous glass matrixes and ignored the influence of the channel walls, do not capture all the factors affecting the thermotropic properties of the embedded nanocrystals.

Introduction

According to classical theory, crystal nuclei become stable and grow into mature crystals upon achieving a critical size, which is governed by the sum of a (positive) surface free energy term that dominates at precritical sizes and a (negative) volume free energy term that dominates growth beyond the critical size.¹ Generally thought to have structures mimicking the crystal packing of their corresponding mature forms, these nuclei determine crystallization outcomes such as crystal size, crystal habit, and polymorphism, the latter pertaining to the ability of a material to adopt different crystal structures. The unique characteristics of nucleation suggest that crystallization in chambers having dimensions near the critical size (typically nanometer-scale) can be regulated systematically by adjustment of the chamber size and shape. Indeed, we recently demonstrated that polymorphism, a crucial issue in numerous material and specialty chemicals, could be regulated during crystallization in the nanoscopic pores of both glass and polymer matrixes.² This effect was attributed to different critical sizes of polymorph nuclei and the size constraints imposed on these nuclei by the ultrasmall pores.

Like crystal nucleation, the surface area/volume ratio can affect the thermotropic properties of very small crystals, particularly at nanometer-scale dimensions. This has prompted a few investigations of the melting behavior of nanometer-sized crystals of metals,^{3,4} ice,⁵ and organic solids.^{6–9} Most of these studies have relied on confinement of the crystals in the channels of nanoporous glass (commonly known as controlled pore glass, or CPG), which results in substantial melting point depression (ΔT_m) due to the constraints on crystal size imposed by the pores. The magnitude of ΔT_m has been found to increase with

decreasing crystal dimensions owing to the increasing contribution from the exposed surface compared with the relatively small volume. This thermotropic behavior has been explained by some in terms of a modified form of the Gibbs–Thomson equation^{10,11} (eq 1), where T_m is the melting temperature of the bulk solid, $T_m(d)$ is the melting temperature of a small cylindrical solid with diameter d , ΔH^{fus} is the molar enthalpy of fusion, ρ_{solid} is the molar density of the solid, and $\gamma_{\text{solid–melt}}$ is the specific free energy for the solid–melt interface. Related, but alternative, expressions that rely on known bulk surface energies of the solid and melt phases have also been used to explain ΔT_m .¹² Equation 1 predicts a linear relationship between the melting point depression and the inverse of the crystal size, which is assumed to be identical with the pore diameter because the pore dimension limits the crystal size. The slope provides a direct measure of $\gamma_{\text{solid–melt}}$ based on the bulk values for ΔH^{fus} and ρ_{solid} . Conversely, given known values of $\gamma_{\text{solid–melt}}$, ΔH^{fus} , and ρ_{solid} or simply a product of these terms determined empirically, the pore diameter can be calculated directly from the melting point depression of a standard reference compound, which is the basis for cryoporometry.¹³ Either analysis, however, relies on certain simplifying assumptions. Specifically, eq 1 ignores contributions from the solid–pore wall and liquid–pore wall interfaces, which seem likely. Because previous melting point depression measurements have been limited largely to porous silica-based materials, the influence of these interfaces on the thermotropic properties of embedded nanocrystals has not been revealed. Furthermore, the use of eq 1 assumes that ΔH^{fus} and ρ_{solid} are independent of crystal size.

$$\Delta T_m = T_m - T_m(d) = \frac{4\gamma_{\text{solid–melt}}T_m}{d\Delta H^{\text{fus}}\rho_{\text{solid}}} \quad (1)$$

* To whom correspondence should be addressed. E-mail: wardx004@umn.edu.

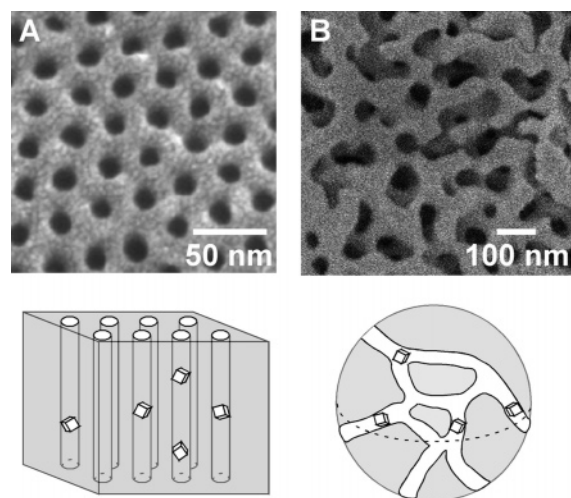


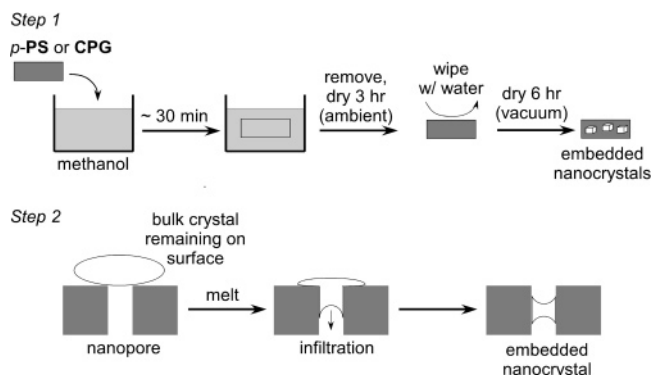
Figure 1. (A) Scanning electron micrograph of a (platinum-coated) p-PS monolith prepared by chemical degradation of the PLA block of a PS–PLA diblock copolymer with an oriented hexagonal cylinder microstructure and a channel diameter $d = 23$ nm. (B) Scanning electron micrograph of CPG (gold-coated) with $d = 55$ nm. Schematic representations of the respective pore structures and nanocrystals grown in the pores are illustrated below the corresponding micrographs.

Recently, we reported the preparation of polystyrene–poly(lactide) (PS–PLA) block copolymer monoliths with hexagonally packed nanocylinders of PLA in PS.¹⁴ Macroscopic shear alignment followed by chemical etching of the PLA produced porous polystyrene (p-PS) monoliths consisting of a PS matrix with oriented hexagonally close-packed nanoscopic channels. The diameter of these channels was highly uniform and could be tuned through control of the component volume fractions and molecular weight. Unlike etchable block copolymer thin films,¹⁵ this method produces macroscopic monoliths with channels that can be imbibed by substantial volumes of liquids, either solvents or molten solids, thereby providing a route to examining crystallization within the channels (Figure 1). These monoliths possess several attractive attributes for studies of crystallization and nanocrystal properties, including (i) precise control of the channel diameter, which may affect the formation of stable nuclei due to critical size effects, (ii) control of the shape of the “chamber” containing embedded nanocrystals, which may influence nucleation and crystal properties by constraining the natural habit of crystal nuclei, and (iii) introduction of functional groups to the channel walls; hydroxyl groups produced naturally during hydrolysis of the PLA block can be subsequently altered through chemical modification.¹⁴ The polymer monoliths, therefore, provide an interesting complement to CPG with respect to examining the role of channel wall surfaces on confined crystallization and the thermotropic properties of embedded nanocrystals. We report herein an investigation of organic nanocrystals embedded in CPG and p-PS that reveals how the melting properties of the embedded nanocrystals are influenced by both the channel diameter and interfacial interactions with the channel walls. Furthermore, we demonstrate that ΔH^{fus} decreases with decreasing channel diameter. Collectively, these observations reveal that eq 1 does not capture all the terms necessary to describe the thermotropic properties of the embedded nanocrystals.

Results and Discussion

The influence of size confinement on crystal properties can be illustrated by the melting behavior of 2,2,3,3,4,4-hexafluoro-1,5-pentanediol [HFPD; $\text{HOCH}_2(\text{CF}_2)_3\text{CH}_2\text{OH}$]¹⁶ and (*R*)-(+)-

SCHEME 1



3-methyladipic acid [R-MAA; $\text{HO}_2\text{CCH}_2\text{CH}(\text{CH}_3)(\text{CH}_2)_2\text{CO}_2\text{H}$] embedded in CPG beads or p-PS. The channel diameters of the PS monoliths were adjusted to values near those of commercially available CPG.^{17,18} The existence of the channels in the monoliths and their diameters were confirmed by small-angle X-ray scattering (SAXS) and scanning electron microscopy (SEM). HFPD and R-MAA were chosen for these investigations because their bulk melting temperatures ($T_{\text{m,HFPD}} = 81$ °C, $T_{\text{m,R-MAA}} = 88$ °C) are below the PS glass transition temperature ($T_{\text{g,PS}} \approx 92$ °C; the exact value depends on molecular weight and thermal scan rate). The channels of the p-PS monoliths collapse near $T_{\text{g,PS}}$,¹⁴ which limits examination of size confinement at higher temperatures (in contrast, the channels of the CPG matrices are stable up to 600 °C). Both HFPD and R-MAA are very soluble in methanol, a nonsolvent for PS, which can be imbibed readily into the CPG beads and p-PS monoliths by capillary action.

Nanocrystals of HFPD were generated in CPG and p-PS either by evaporation of methanol solutions that had been imbibed into the porous hosts or by cooling of an imbibed melt, which also filled the channels readily by capillary action (step 1, Scheme 1). The amount of nanocrystal loading achieved by imbibing methanol solutions of HFPD was approximately 30 wt %. Substantially larger loadings were achieved by imbibing molten HFPD, the amount increasing with increasing pore volume in the PS monolith.¹⁹ Molten R-MAA did not readily infiltrate the CPG or p-PS channels, despite its ability to wet glass surfaces (contact angle $\approx 14^\circ$). This was attributed to the large viscosity of molten R-MAA, which was 45 cP at 92 °C compared with 18 cP for molten HFPD at 85 °C [the viscosity of each compound was measured at 4 °C above its respective melting point, the same temperature used to melt the bulk nanocrystals on the external surfaces in the differential scanning calorimetry (DSC) measurements]. In principle, HFPD and R-MAA on the external surfaces of the impregnated p-PS monoliths could be removed without affecting the embedded nanocrystals by shaking in water (both compounds are soluble in water), which does not effectively penetrate the channels. This procedure, however, often resulted in fracture of the monoliths as a result of their mechanical fragility. Therefore, the impregnated p-PS monoliths were wiped carefully with a water-soaked cloth to remove the bulk HFPD and R-MAA from the outer surfaces. The small size of the CPG beads precluded removal of external bulk crystals with this method. Furthermore, the external crystals could not be removed by simply immersing the beads in water because water penetrates the channels and promotes extraction of the embedded nanocrystals. In the case of HFPD, any small amount remaining on the outer surfaces of the CPG or p-PS was readily absorbed into the channels through capillary action upon increasing the temperature of impregnated

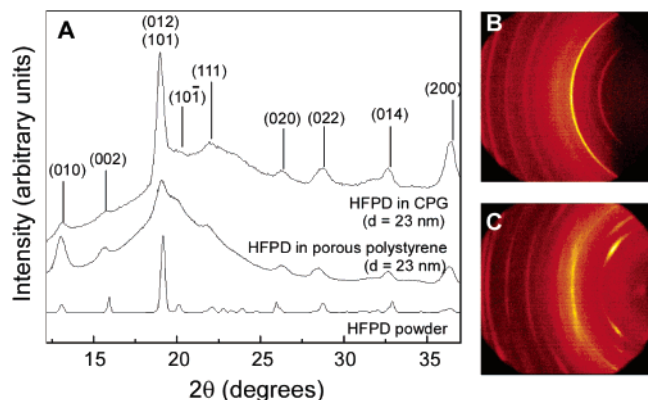


Figure 2. (A) Illustrative X-ray microdiffraction data for HFPD nanocrystals embedded in p-PS and CPG, at room temperature. The diffraction pattern for bulk HFPD powder is illustrated for comparison. The channel diameter (d) of the host matrices is indicated below each diffraction pattern. The peaks were indexed on the basis of powder diffraction patterns calculated from the single-crystal structure of the room-temperature polymorph of HFPD. Broad amorphous backgrounds underneath the HFPD peaks are evident for both p-PS and CPG. (B) Two-dimensional X-ray microdiffraction patterns for HFPD nanocrystals embedded in 23-nm CPG and (C) in 23-nm p-PS. The crystals in both matrices were grown by evaporation of imbibed methanol solutions.

materials slightly above the melting point of HFPD (step 2, Scheme 1). This treatment resulted in the disappearance of thermal signatures associated with bulk HFPD. Because molten R-MAA could not penetrate the channels of either CPG or p-PS, it was difficult to remove trace amounts of this compound from the external surfaces using this heating protocol. The presence of bulk crystals on the outer surface, however, did not appreciably affect the melting behavior of the embedded nanocrystals, which had thermal signatures that were distinct from those of the bulk crystals.

The formation of HFPD nanocrystals inside p-PS and CPG was confirmed by X-ray microdiffraction, which revealed peaks at 2θ values coinciding with those of the room-temperature polymorph of HFPD (Figure 2).²⁰ The nanocrystal peaks were indexed on the basis of diffraction patterns calculated from the single-crystal structure of this polymorph. The diffraction peaks of the embedded nanocrystals were noticeably broader than those of bulk HFPD, and the full width at half-maximum (fwhm) decreased with increasing channel diameter. When the fwhm values and the Scherrer equation were used,²¹ the calculated nanocrystal sizes were found to be comparable with the channel diameter. For example, CPG and p-PS with 23-nm channels afforded 19- and 18-nm crystals, respectively.²² This clearly indicates that the sizes of the nanocrystals are limited by the channel diameter, which in turn limits growth of the crystals along the channel length due to the natural constraints imposed by the inherent crystal morphology. Interestingly, the two-dimensional X-ray microdiffraction patterns for HFPD in p-PS suggested some degree of preferred orientation. Analysis of the two-dimensional pattern was consistent with the (012) plane roughly parallel with the channel walls. Notably, this plane contains layers of HFPD molecules associated by in-plane hydrogen bonds, such that only the nonpolar CF_2 groups protrude from its surface. Therefore, this orientation would minimize the contact of the polar hydroxyl groups with the p-PS pore walls. It is not possible to detect preferred orientation in the channels of CPG because, unlike the p-PS monolith, the CPG beads cannot be aligned in the X-ray beam.

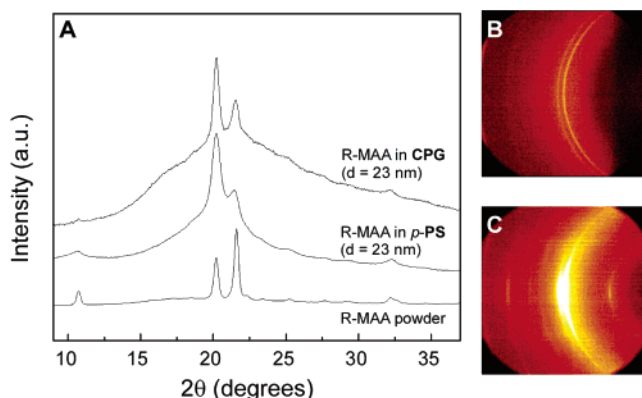


Figure 3. (A) One-dimensional X-ray microdiffraction data for crystals in 23-nm p-PS and 23-nm CPG. (B) Two-dimensional X-ray microdiffraction pattern for R-MAA nanocrystals embedded in 23-nm CPG and (C) in 23-nm p-PS. The weak reflections above and below the horizon and the strong reflections along the horizon are consistent with some preferred orientation of the nanocrystals in the p-PS channels. The crystals in both matrices were grown by evaporation of imbibed methanol solutions.

The crystal structure of R-MAA is not known, and attempts in our laboratory to grow crystals suitable for single-crystal X-ray diffraction have been unsuccessful. Nonetheless, X-ray microdiffraction of impregnated CPG and p-PS revealed powder patterns that could be assigned to crystalline R-MAA embedded in the channels. Upon evaporation of the imbibed methanol solutions, the powder pattern exhibited only one prominent peak at $2\theta = 20.3^\circ$, which was identical with one of the diffraction peaks observed for bulk R-MAA crystallized from methanol. If the imbibed R-MAA was melted and then cooled ($5^\circ\text{C}/\text{min}$), the powder pattern revealed the presence of a new polymorph, which was also obtained if bulk R-MAA was formed by cooling of its melt (Figure 3). Like HFPD, the diffraction peaks of the embedded nanocrystals were broader than those of the bulk, and the fwhm decreased with increasing channel diameter. When the fwhm values and the Scherrer equation were used, the calculated nanocrystal dimensions were found to be comparable with the channel diameter. For example, dimensions of the R-MAA nanocrystals formed by cooling molten R-MAA in the channels of 23-nm CPG and p-PS were 30 and 24 nm, respectively.²² Some preferred orientation of the R-MAA crystals in p-PS also was apparent.

The melting behaviors of embedded HFPD and R-MAA crystals were diagnostic of their nanometer-scale dimensions, with melting points substantially lower than that of bulk HFPD and R-MAA (Figure 4). This melting point depression resembles that observed for metals,^{3,4} ice,⁵ and organic solids⁶ embedded in porous silica or CPG with channel diameters <100 nm. The melting features of the embedded HFPD crystals were independent of whether the porous hosts were impregnated from methanol solutions or the melts. The melting point of the HFPD nanocrystals decreased with decreasing channel diameter, achieving values of $T_m = 69.9 \pm 3.0^\circ\text{C}$ and $64.3 \pm 3.0^\circ\text{C}$ in 23-nm CPG and p-PS, respectively. The melting point was depressed even further in 7.5-nm CPG (this channel diameter is difficult to obtain in p-PS). The melting point approaches the bulk value of $T_{m,\text{HFPD}} = 81^\circ\text{C}$ as the channel diameter was increased. Whereas DSC revealed one predominant endotherm during melting in p-PS, multiple endotherms were observed for HFPD melting in CPG. This behavior can be reasonably associated with multiple crystal sizes in CPG that result from nonuniform pores²³ or branching defects that produce regions with local pore dimensions exceeding the average size. In

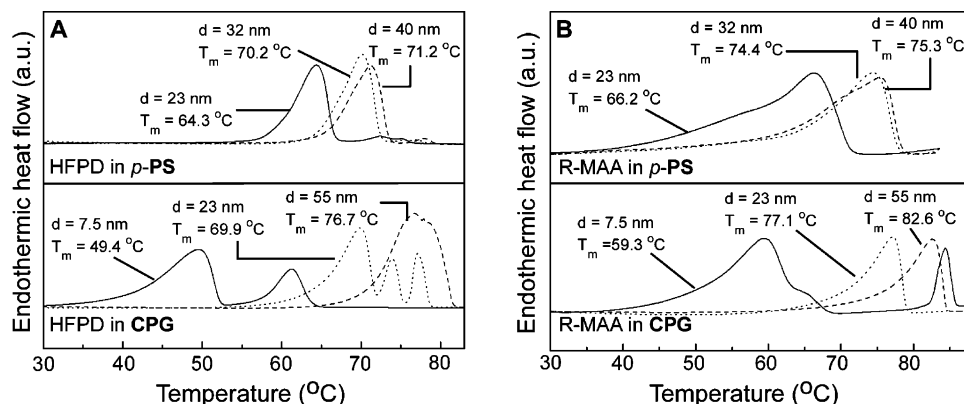


Figure 4. DSC data (scan rate = $5^\circ\text{C}/\text{min}$) for (A) HFPD and (B) R-MAA nanocrystals, initially grown by evaporation of imbibed methanol solutions (50% w/w) in p-PS monoliths and CPG having various channel diameters (d). The data shown here were collected on the second DSC scan, after the crystals had been subjected to one melting and cooling cycle.

contrast, the single endotherm observed for p-PS suggests a more uniform pore structure, consistent with SAXS and SEM characterization.¹⁴ Nanocrystals of R-MAA behaved somewhat differently. Broad endotherms were observed in p-PS, suggesting a distribution of crystal sizes. Multiple endotherms were absent in 23- and 55-nm CPG samples, but the 7.5-nm CPG samples exhibited the bulk melting peak, which can be attributed to bulk R-MAA remaining on the external surfaces, and a small shoulder on the high-temperature side of a broad endotherm near 60°C . Like HFPD, the melting points of R-MAA nanocrystals were higher in CPG; $T_m = 77.1 \pm 2.0^\circ\text{C}$ and $66.2 \pm 4.0^\circ\text{C}$ for 23-nm CPG and p-PS, respectively. The different nanocrystal melting points in the CPG and p-PS data indicate that the thermotropic behavior of the embedded nanocrystals depends on the nanocrystal/matrix combination. This can be attributed to either (i) different wetting of the internal pore walls of the two materials by the embedded nanocrystals and their melts or (ii) differences in the ability of the melts to recrystallize in branching defects of CPG and p-PS.

The melting behavior of HFPD was examined using variable-temperature X-ray microdiffraction, which revealed the complete disappearance of diffraction peaks upon melting at the temperatures expected from the DSC data. Because of the nonuniform crystal sizes in CPG, the fwhm of the diffraction peaks associated with the HFPD nanocrystals decreased upon heating owing to the successive melting of the embedded HFPD nanocrystals in order of increasing size (Figure 5).

The melting point depression, ΔT_m , exhibited by crystals confined within nanoscopic channels (Scheme 2) has been evaluated previously in terms of a modified and simplistic form of the Gibbs–Thomson equation^{10,11} (eq 1). Equation 1 predicts a linear relationship between ΔT_m and $1/d$ (d typically is assumed to be identical with the channel diameter). Although eq 1 has been useful in this regard, it is actually a simplified form that ignores the energy terms associated with the solid–substrate (solid–sub) and liquid melt–substrate (melt–sub) interfaces, where the substrate is the channel wall. The Gibbs–Thomson equation is represented more accurately by eq 2 or its equivalent form (eq 3), which reveals these surface energy terms (see Appendix for a complete derivation, including the terms in Scheme 2). Inspection of these equations reveals that eq 1 assumes that θ , the contact angle of the solid with the channel wall, is 180° . Under these conditions, the solid nanocrystals would have no contact with the wall, which seems unrealistic. To our knowledge, however, this assumption has never been tested experimentally because studies of the thermotropic properties of crystals embedded in nanoscopic

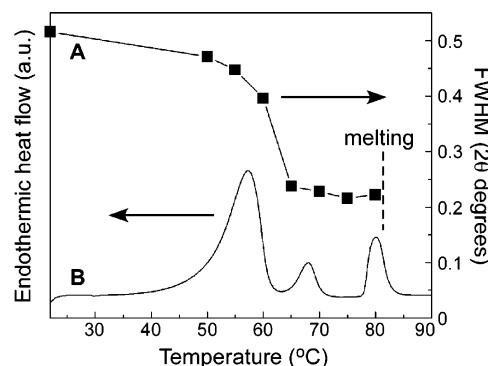
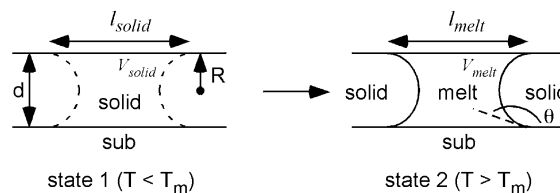


Figure 5. (A) fwhm of the (010) peak of HFPD embedded in 7.5-nm CPG during heating from room temperature to above the bulk melting point. The fwhm was calculated from the data after baseline correction of the X-ray diffraction data and fitting the (010) peak to a Gaussian line shape. (B) DSC data for the same sample (scan rate = $5^\circ\text{C}/\text{min}$). The peak at 81°C is due to bulk HFPD remaining on the external surfaces of the CPG.

SCHEME 2



channels generally have been limited to porous glasses such as CPG.

$$\frac{\Delta T_m}{T_m} = -\frac{4\gamma_{\text{solid-melt}}}{\rho_{\text{solid}}\Delta H_{\text{fus}}d} \cos \theta \quad (2)$$

$$\frac{\Delta T_m}{T_m} = \frac{4}{\rho_{\text{solid}}\Delta H_{\text{fus}}d} (\gamma_{\text{solid-sub}} - \gamma_{\text{melt-sub}}) \quad (3)$$

The effect of different porous host materials is immediately evident from a comparison of the dependence of $\Delta T_m/T_m$ on $1/d$ for HFPD and R-MAA nanocrystals in CPG and p-PS (Figure 6). Though the data are limited to only a few channel diameters, the linearity expected from eqs 1–3 is evident. The HFPD data indicates that the slopes are independent of the method used to imbibe HFPD (solution or melt). The slopes of the data, given by eq A18, were measurably steeper for the p-PS matrix than for CPG. The data for HFPD reveal that the effect

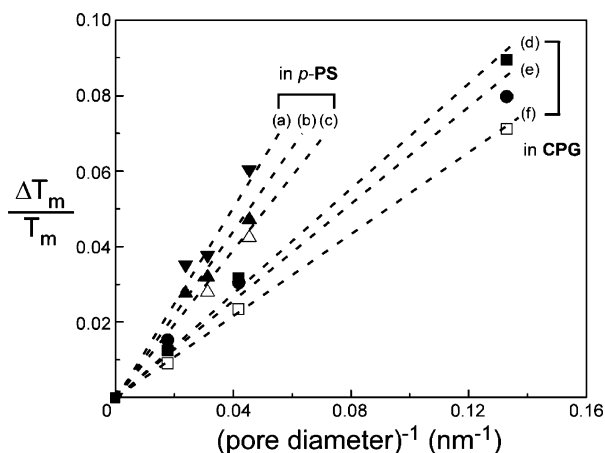


Figure 6. Dependence of the normalized melting point depression, $\Delta T_m/T_m$, on the channel diameter for (a, \blacktriangledown) R-MAA in p-PS, imbibed from methanol, (b, \blacktriangle) HFPD in p-PS, (c, \triangle) HFPD in p-PS, imbibed from melt, (d, \blacksquare) HFPD in CPG, imbibed from methanol, (e, \bullet) R-MAA in CPG, imbibed from methanol, and (f, \square) HFPD in CPG imbibed from melt. The slopes are larger for the p-PS monoliths. The data for HFPD reveal that the effect of the porous matrix outweighs the differences arising from the method used to introduce the HFPD to the channels (melt or methanol solutions). The dashed lines represent the best fit to each data set, including a point added at $\Delta T_m/T_m = 0$, $1/d = 0$, that corresponds to the bulk melting temperature.

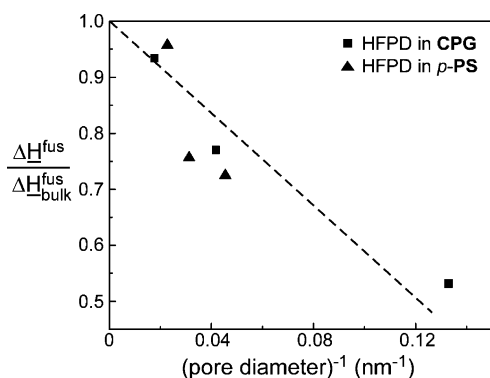


Figure 7. Dependence of the latent heat of fusion for HFPD in CPG and p-PS with various channel diameters.

of the porous matrix outweighs the differences arising from the method used to introduce the HFPD to the channels (melt or methanol solutions). Clearly, the composition of the porous matrix as well as the size of its pores influences the thermotropic properties of the embedded nanocrystals.

If the simplified form represented by eq 1 is assumed valid and the experimentally measured values of $\Delta \hat{H}^{\text{fus}} = 29.7$ kJ/mol ($\Delta \hat{H}^{\text{fus}} = 140$ J/g) for bulk HFPD and $\rho_{\text{solid}} = 8709$ mol/m³ (or 1.847 g/cm³) are used, these data would require substantially different $\gamma_{\text{solid-melt}}$ values in the two porous hosts ($\gamma_{\text{solid-melt}} = 34$ mJ/m² in CPG and 63 mJ/m² HFPD in p-PS). This is unrealistic and indicates that eq 1 does not account fully for the influence of the surface. Specifically, it argues that the $\cos \theta$ term in eq A16b, which reflects interfacial interactions with the channel wall, cannot be ignored.²⁴ On the basis of eq 2, the steeper slopes in Figure 5 for nanocrystals embedded in p-PS suggest that, compared with CPG, the interfacial energy of the solid with the pore walls of PS is lower than that of its melt. Furthermore, DSC measurements revealed that $\Delta \hat{H}^{\text{fus}}$ of the embedded nanocrystals (see experimental section) decreased with decreasing crystal size (Figure 7), in agreement with behavior reported previously for organic solids embedded in CPG.^{7,8} Despite this property, the data in Figure 6 are reasonably

linear, suggesting that the reduction in $\Delta \hat{H}^{\text{fus}}$, which should be independent of the composition of the porous matrix, was fortuitously compensated by a reduction in the magnitude of the $(\gamma_{\text{solid-sub}} - \gamma_{\text{melt-sub}})$ term of eq 3. This is not entirely unexpected, because the surface energy of the crystal is expected to approach that of the liquid with decreasing crystal size, thereby reducing the magnitude of $(\gamma_{\text{solid-sub}} - \gamma_{\text{melt-sub}})$.²⁵ Clearly, the simplified approach to explaining the melting behavior of embedded crystals using eq 1 does not properly capture all the terms necessary to describe the thermotropic properties of the embedded nanocrystals.

Summary

The results described here demonstrate that the melting behavior of organic nanocrystals, grown and confined in nanoscopic channels of p-PS and CPG, is influenced strongly by the channel diameter, with the melting point depression scaling inversely with crystal size. The sizes of the nanocrystals are limited by the channel diameter, which in turn limits growth of the crystals along the channel length as a result of the natural constraints imposed by the inherent crystal morphology. More importantly, the results clearly reveal that the melting behavior is influenced by the matrix material, with p-PS exerting a more pronounced effect on the melting point depression than the silica-based CPG. Furthermore, the enthalpy of fusion decreases with crystal size. The X-ray microdiffraction data reveal a preferred orientation for HFPD nanocrystals embedded in p-PS, which suggests favorable wetting of the pore walls by certain crystal planes. Collectively, these phenomena indicate that simplifying assumptions used previously to describe the thermotropic properties of organic nanocrystals do not capture all the terms necessary to characterize the behavior associated with the nanoscale dimensions of the crystals and their interaction with the channel walls of the embedding matrix.

Experimental Section

Materials. HFPD and R-MAA were purchased from Sigma-Aldrich (Milwaukee, WI) and used without further purification. CPG was purchased from CPG, Inc. (Lincoln Park, NJ). CPG was treated with boiling nitric acid for several hours to remove any possible contaminants, washed with deionized water, and dried for 12 h under a vacuum. The acid-washed CPG was stored under air in a desiccator. This treatment has little effect on the channel dimensions.²⁶ p-PS was prepared by first pressing a powder of a PS-PLA diblock copolymer in a mold at 115–140 °C and 1000 psi using a laboratory press, which upon cooling to room temperature afforded a chunk of compressed polymer. This was then added to a channel die (3 mm wide \times 60 mm long) at 115–140 °C and subjected to compression for approximately 1 h, causing the polymer to flow toward the ends of the channels. Typical compression ratios ranged from 6 to 15. This process resulted in alignment of the hexagonal cylindrical microstructure, with PLA cylinders, in the PS matrix, aligned parallel to the channel. The aligned PS-PLA diblock copolymer was allowed to cool to room temperature under ambient conditions. The PLA component then was etched by immersing the aligned diblock copolymer in a 60:40 water/methanol mixture (by volume) containing 0.5 M NaOH and heating to 65 °C for 7–14 days. The etched polymer monoliths then were washed with a 60:40 water/methanol mixture (no NaOH) and dried for 12 h at room temperature under a vacuum.¹⁴ The p-PS monoliths and CPG beads were characterized with SEM (JEOL 6500 and Hitachi S-900 FE-SEM, University of Minnesota), which permitted direct visualization

of the channels at the surface. The existence of internal porosity in p-PS was confirmed by SEM characterization of fractured monoliths. The channel dimensions of the various p-PS monoliths were corroborated from the d spacings measured with SAXS (X-ray facility, University of Minnesota) and the known volume fraction of PLA in the PS-PLA diblock copolymer.¹⁴ The viscosities of HPFD and R-MAA were measured in the University of Minnesota Rheology Laboratory with an ARES II rheometer (Rheometric Science) in a parallel plate geometry.

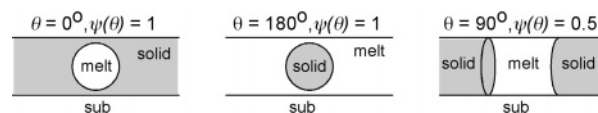
Crystallization of HPFD and R-MAA in Nanoscopic Channels. The p-PS monoliths or CPG beads were immersed in methanol solutions containing either HPFD or R-MAA in 50% (w/w). Initially, the empty p-PS monoliths and CPG beads were opaque, but they became translucent within approximately 30 min because of infiltration of the methanol solution. After this treatment, the p-PS monoliths and CPG beads were removed from the solution and allowed to dry under ambient conditions for 3 h to allow for crystallization in the channels. Crystals of HPFD or R-MAA on the external surfaces of the p-PS monoliths were removed by carefully wiping the surfaces with a wet cloth. The p-PS monoliths were dried in a vacuum for 6 h. The infiltrated CPG materials were not amenable to the same cleaning procedures. Therefore, they were simply dried in a vacuum for 6 h after the ambient drying step. The embedded nanocrystals were characterized with wide-angle X-ray diffraction using a Bruker-AXS microdiffractometer available in the Characterization Facility, University of Minnesota. The monoliths were aligned in a fixed orientation with the long axes of the cylindrical pores perpendicular to the incident beam. The thermotropic properties of the embedded nanocrystals were characterized with DSC (Pyris-1, Perkin-Elmer, or Q1000, TA Instruments). The molar enthalpies of fusion of the embedded nanocrystals, $\Delta H_{\text{fus}}^{\text{solid}}$, were determined from DSC data collected for p-PS and CPG samples treated with an excess amount of molten HPFD in the DSC pan. The samples were cooled to room temperature and then subjected to another heating cycle in the DSC. The mass of the external bulk HPFD was calculated from the integrated intensity of the bulk melting endotherm and the known molar enthalpy of fusion for the bulk material ($\Delta H_{\text{bulk}}^{\text{fus}} = 29.7$ kJ/mol).

Acknowledgment. This work was supported primarily by the MRSEC Program of the National Science Foundation under Award No. DMR-0212302. Small-angle and wide-angle X-ray scattering was performed in the University of Minnesota Institute of Technology Characterization Facility. The authors thank Dr. Victor G. Young, Jr., and the X-ray Crystallographic Laboratory in the Department of Chemistry at the University of Minnesota for assistance with single-crystal X-ray structural analysis, and they gratefully acknowledge the assistance of Ms. Johanna H. Wolf in the preparation of the block copolymer monoliths.

Appendix

The thermotropic behavior of the embedded crystalline solids described in the accompanying manuscript can be viewed by the configuration in Scheme 2, in which a solid is in contact with the walls of a cylindrical channel (substrate), with radius R , prior to melting, which is denoted as state 1 ($T < T_m$). A reference volume, V_{solid} , can be defined as the volume of solid that will become a melt upon heating. This reference volume (defined by the dashed lines) is related by eq A1a to an effective length, l'_{solid} , that accounts for the shape of the interface that will be formed between the solid and melt upon heating. If the

SCHEME 3



temperature is increased to $T > T_m$, this reference volume melts and the volume of the resulting liquid, V_{melt} , is related by eq A1b to a new effective length, l'_{melt} , which may differ from l'_{solid} if the densities of the solid and melt are different. The corresponding solid-substrate and liquid-substrate interfaces have lengths l_{solid} and l_{melt} , respectively. Therefore, the free energies of state 1 and state 2 are described by eqs A2 and A3, where ρ_{solid} and ρ_{melt} are the solid and liquid molar densities, G_{solid} and G_{melt} are the solid and liquid specific volume free energies (on a molar basis), $\gamma_{\text{solid-sub}}$ and $\gamma_{\text{melt-sub}}$ are the specific interfacial energies of the solid-substrate and liquid-substrate interfaces, $\gamma_{\text{solid-melt}}$ is the specific interfacial energy of the solid-liquid interface, and $\psi(\theta) = 1/(1 + \sin \theta)$ is a shape factor that describes the curvature of the solid-liquid interface based on the contact angle θ . The value of $\psi(\theta)$ assumes a value of $\psi(\theta) = 1$ for $\theta = 0$ or 180° and $\psi(\theta) = 0.5$ for $\theta = 90^\circ$. These specific conditions describe a liquid sphere surrounded by the solid [$\psi(\theta) = 1$, $\theta = 0^\circ$], a solid sphere surrounded by the liquid melt [$\psi(\theta) = 1$, $\theta = 180^\circ$], and the liquid melt trapped between two solid disks [$\psi(\theta) = 0.5$, $\theta = 90^\circ$], as illustrated in Scheme 3.

$$l'_{\text{solid}} = \frac{V_{\text{solid}}}{\pi R^2} \quad (\text{A1a})$$

$$l'_{\text{melt}} = \frac{V_{\text{melt}}}{\pi R^2} \quad (\text{A1b})$$

$$G_1 = \pi R^2 l'_{\text{solid}} \rho_{\text{solid}} \underline{G}_{\text{solid}} + 2\pi R l_{\text{solid}} \gamma_{\text{solid-sub}} \quad (\text{A2})$$

$$G_2 = \pi R^2 l'_{\text{melt}} \rho_{\text{melt}} \underline{G}_{\text{melt}} + 2\pi R l_{\text{melt}} \gamma_{\text{melt-sub}} + \psi(\theta) 4\pi R^2 \gamma_{\text{solid-melt}} \quad (\text{A3})$$

If the molar volumes of the solid and liquid phases are identical (i.e., $\rho_{\text{solid}} = \rho_{\text{melt}}$), then $l'_{\text{solid}} = l'_{\text{melt}} = l'$ and the free energy change associated with the transformation from state 1 to state 2 (melting) is given by eq A4.

$$\Delta G = G_2 - G_1 = \pi R^2 l' (\rho_{\text{melt}} \underline{G}_{\text{melt}} - \rho_{\text{solid}} \underline{G}_{\text{solid}}) + 2\pi R l_{\text{melt}} \gamma_{\text{melt-sub}} - 2\pi R l_{\text{solid}} \gamma_{\text{solid-sub}} + \psi(\theta) 4\pi R^2 \gamma_{\text{solid-melt}} \quad (\text{A4})$$

If it is also assumed that $l_{\text{solid}} = l_{\text{melt}} = l$, then the free energy change can be described by eq A5.

$$\Delta G = \pi R^2 l' \rho_{\text{solid}} (\underline{G}_{\text{melt}} - \underline{G}_{\text{solid}}) + 2\pi R l (\gamma_{\text{melt-sub}} - \gamma_{\text{solid-sub}}) + \psi(\theta) 4\pi R^2 \gamma_{\text{solid-melt}} \quad (\text{A5})$$

On the basis of the Gibbs-Helmholtz relationship (eq A6), where $\Delta T_m = T_m - T_m(d)$, where T_m is the bulk melting temperature and $T_m(d)$ is the melting temperature of a crystal with size d ($d = 2R$), and the relationship between the contact angle and the interfacial energies (eq A7), the free energy change can be described by eq A8.

$$\underline{G}_{\text{melt}} - \underline{G}_{\text{solid}} = \Delta \underline{H}^{\text{fus}} \frac{\Delta T_{\text{m}}}{T_{\text{m}}} \quad (\text{A6})$$

$$\cos \theta = \frac{\gamma_{\text{melt-sub}} - \gamma_{\text{solid-sub}}}{\gamma_{\text{solid-melt}}} \quad (\text{A7})$$

$$\Delta G = \pi R^2 l' \rho_{\text{solid}} \Delta \underline{H}^{\text{fus}} \frac{\Delta T_{\text{m}}}{T_{\text{m}}} + 2\pi R l (\cos \theta) \gamma_{\text{solid-melt}} + \psi(\theta) 4\pi R^2 \gamma_{\text{solid-melt}} \quad (\text{A8})$$

At the equilibrium melting point $\Delta G = 0$

$$\Delta G = \pi R^2 l' \rho_{\text{solid}} \Delta \underline{H}^{\text{fus}} \frac{\Delta T_{\text{m}}}{T_{\text{m}}} + 2\pi R l (\cos \theta) \gamma_{\text{solid-melt}} + \psi(\theta) 4\pi R^2 \gamma_{\text{solid-melt}} = 0 \quad (\text{A9})$$

Dividing both sides by πR ,

$$R l' \rho_{\text{solid}} \Delta \underline{H}^{\text{fus}} \frac{\Delta T_{\text{m}}}{T_{\text{m}}} + 2l (\cos \theta) \gamma_{\text{solid-melt}} + \psi(\theta) 4R \gamma_{\text{solid-melt}} = 0 \quad (\text{A10})$$

Rearranging

$$R l' \rho_{\text{solid}} \Delta \underline{H}^{\text{fus}} \frac{\Delta T_{\text{m}}}{T_{\text{m}}} = -2l (\cos \theta) \gamma_{\text{solid-melt}} - \psi(\theta) 4R \gamma_{\text{solid-melt}} \quad (\text{A11})$$

We note here that

$$\text{if } \gamma_{\text{melt-sub}} > \gamma_{\text{solid-sub}}, \quad 1 > \cos \theta > 0 \quad (0^\circ < \theta < 90^\circ; \text{ i.e., the solid wets the substrate})$$

$$\text{if } \gamma_{\text{melt-sub}} < \gamma_{\text{solid-sub}}, \quad 0 > \cos \theta > -1 \quad (90^\circ < \theta < 180^\circ; \text{ i.e., the liquid wets the substrate})$$

Rearranging

$$\frac{\Delta T_{\text{m}}}{T_{\text{m}}} = -\frac{2l (\cos \theta) \gamma_{\text{solid-melt}}}{R l' \rho_{\text{solid}} \Delta \underline{H}^{\text{fus}}} - \frac{\psi(\theta) 4 \gamma_{\text{solid-melt}}}{l' \rho_{\text{solid}} \Delta \underline{H}^{\text{fus}}} \quad (\text{A12})$$

Rearranging

$$\Delta T_{\text{m}} = -\frac{2l (\cos \theta) \gamma_{\text{solid-melt}} T_{\text{m}}}{R l' \rho_{\text{solid}} \Delta \underline{H}^{\text{fus}}} - \frac{\psi(\theta) 4 \gamma_{\text{solid-melt}} T_{\text{m}}}{l' \rho_{\text{solid}} \Delta \underline{H}^{\text{fus}}} \quad (\text{A13a})$$

$$\Delta T_{\text{m}} = -\frac{4l \gamma_{\text{solid-melt}} T_{\text{m}} \cos \theta}{l' \rho_{\text{solid}} \Delta \underline{H}^{\text{fus}} 2R} - \frac{\psi(\theta) 4 \gamma_{\text{solid-melt}} T_{\text{m}}}{l' \rho_{\text{solid}} \Delta \underline{H}^{\text{fus}}} \quad (\text{A13b})$$

If we assume that the solid crystal is a long cylinder and that the lengths of the reference volume for the solid and liquid are identical, then $l = l' \gg R$, and the second term in eq A12 can be ignored to give

$$\frac{\Delta T_{\text{m}}}{T_{\text{m}}} = -\frac{4 \gamma_{\text{solid-melt}} \cos \theta}{\rho_{\text{solid}} \Delta \underline{H}^{\text{fus}} 2R} \quad (\text{A14})$$

The often-used form of the Gibbs–Thomson equation assumes that $\theta = 180^\circ$; that is, the solid is in contact with the liquid only and does not contact the substrate. Under this highly

idealized condition, the standard form of the Gibbs–Thomson equation is given by eq A15, where the diameter of the channel is $d = 2R$.

$$\Delta T_{\text{m}} = +\frac{4 \gamma_{\text{solid-melt}} T_{\text{m}}}{\rho_{\text{solid}} \Delta \underline{H}^{\text{fus}} 2R} = +\frac{4 \gamma_{\text{solid-melt}} T_{\text{m}}}{\rho_{\text{solid}} \Delta \underline{H}^{\text{fus}} d} \quad (\text{A15})$$

If we consider the more general case of $\theta \neq 180^\circ$,

$$\Delta T_{\text{m}} = -\frac{4 \gamma_{\text{solid-melt}} T_{\text{m}}}{\rho_{\text{solid}} \Delta \underline{H}^{\text{fus}} d} \cos \theta \quad (\text{A16a})$$

$$\frac{\Delta T_{\text{m}}}{T_{\text{m}}} = -\frac{4 \gamma_{\text{solid-melt}}}{\rho_{\text{solid}} \Delta \underline{H}^{\text{fus}} d} \cos \theta \quad (\text{A16b})$$

Recalling that $\Delta T_{\text{m}} = T_{\text{m}} - T_{\text{m}}(d)$, if $0^\circ < \theta < 90^\circ$ ($1 > \cos \theta > 0$) eq A16a produces a negative ΔT_{m} , which is tantamount to raising the melting point (i.e., the solid wets the substrate better than the liquid, thereby inhibiting melting). Conversely, if $90^\circ < \theta < 180^\circ$ ($0 > \cos \theta > -1$), eq A16a produces a positive ΔT_{m} , which is tantamount to melting point depression (i.e., the liquid wets the substrate better than the solid, thereby promoting melting). Recalling eq A7, we find that melting point depression occurs when $\gamma_{\text{melt-sub}} < \gamma_{\text{solid-sub}}$.

$$\frac{\Delta T_{\text{m}}}{T_{\text{m}}} = \frac{4}{\rho_{\text{solid}} \Delta \underline{H}^{\text{fus}} d} (\gamma_{\text{solid-sub}} - \gamma_{\text{melt-sub}}) \quad (\text{A17})$$

Therefore, a plot of $\Delta T/T_{\text{m}}$ versus $1/d$ has the slope

$$\text{slope} = \frac{4}{\rho_{\text{solid}} \Delta \underline{H}^{\text{fus}}} (\gamma_{\text{solid-sub}} - \gamma_{\text{melt-sub}}) \quad (\text{A18})$$

References and Notes

- (1) Oxtoby, D. W. *Acc. Chem. Res.* **1998**, *31*, 91–97.
- (2) Ha, J.-M.; Wolf, J. H.; Hillmyer, M. A.; Ward, M. D. *J. Am. Chem. Soc.* **2004**, *126*, 3382–3383.
- (3) Borisov, B. F.; Charnaya, E. V.; Hoffmann, W. D.; Michel, D.; Shelyapin, A. V.; Kumzerov, Yu. A. *J. Phys.: Condens. Matter* **1997**, *9*, 3377–3386.
- (4) Buffat, Ph.; Borel, J.-P. *Phys. Rev. A* **1976**, *13*, 2287–2298.
- (5) Reinnie, G. K.; Clifford, J. J. *Chem. Soc., Faraday Trans. 1* **1977**, *73*, 680–689.
- (6) Jackson, C. L.; McKenna, G. B. *Chem. Mater.* **1996**, *8*, 2128–2137.
- (7) Jackson, C. L.; McKenna, G. B. *J. Chem. Phys.* **1990**, *93*, 9002–9011.
- (8) Patrick, W. A.; Kemper, W. A. *J. Phys. Chem.* **1938**, *42*, 369–380.
- (9) Hodgson, C.; McIntosh, R. *Can. J. Chem.* **1960**, *38*, 958–971.
- (10) Gibbs, J. W. *The Collected Works of J. Willard Gibbs*; Yale University Press: New Haven, 1928.
- (11) Defay, R.; Prigogine, I. *Surface Tension and Adsorption*; Longmans: London, 1966.
- (12) The melting point depression of nanocrystals has also been explained by an equation similar in form to eq 1 but requiring the surface energies of the solid and melt, γ_{solid} and γ_{melt} , respectively: $T_{\text{m}} - T_{\text{m}}(d) = [4T_{\text{m}}/(\Delta \underline{H}^{\text{fus}} \rho_{\text{solid}} d)] [\gamma_{\text{solid}} - \gamma_{\text{liquid}} (\rho_{\text{solid}}/\rho_{\text{liquid}})^{2/3}]$. See ref 4 and Goldstein, A. N.; Echer, C. M.; Alivisatos, A. P. *Science* **1992**, *256*, 1425–1427.
- (13) Valckenborg, R. M. E.; Pel, L.; Kopinga, K. *J. Phys. D.: Appl. Phys.* **2002**, *35*, 249–256.
- (14) Zalusky, A. S.; Olayo-Valles, R.; Wolf, J. H.; Hillmyer, M. A. *J. Am. Chem. Soc.* **2002**, *124*, 12761–12773.
- (15) Thurn-Albrecht, T.; Schotter, J.; Kästle, G. A.; Emley, N.; Shibuchi, T.; Krusin-Elbaum, L.; Guarini, K.; Black, C. T.; Tuominen, M. T.; Russell, T. P. *Science* **2000**, *290*, 2126–2129.
- (16) HFDP is a precursor to a fluorinated polymer. See Johncock, P.; Hewins, M. A. *H. J. Polym. Sci., Part A: Polym. Chem.* **1975**, *13*, 807–814.
- (17) Haller, W. *Nature* **1965**, *206*, 693–696.

(18) The CPG used here was obtained from CPG, Inc., Lincoln Park, NJ. CPG is prepared from borate-silicate composite glass from which the borate phase is leached to produce a silica glass with uniform pores.

(19) The amount of HFPD loading when imbibed from the melt ranged from 70 to 120 wt % in p-PS and 70–170 wt % in CPG, the larger values achieved for the largest pore sizes. These values are consistent with nearly complete loading of the available pore volume.

(20) Ha, J.-M.; Young V. G. Unpublished results. Single-crystal X-ray diffraction demonstrated that HFPD actually exhibits two polymorphs, one at room temperature (form I, space group $P1$, $a = 4.939$ Å, $b = 6.891$ Å, $c = 11.348$ Å, $\alpha = 81.86^\circ$, $\beta = 86.06^\circ$, $\gamma = 86.78^\circ$, $V_{\text{cell}} = 381.4$ Å³, $Z = 2$, 298 K) and the other at low temperature (form II, $P1$, $a = 4.864$ Å, $b = 5.744$ Å, $c = 13.341$ Å, $\alpha = 82.818^\circ$, $\beta = 87.288^\circ$, $\gamma = 86.344^\circ$, $V_{\text{cell}} = 368.0$ Å³, $Z = 2$, 173 K).

(21) The dimensions of the embedded nanocrystals can be estimated by the Scherrer equation, $d = K\lambda/(B_c \cos \theta)$, where d is the crystal diameter, K is the Scherrer constant (usually assumed to be 0.9), λ is the X-ray wavelength, B_c is the corrected peak width at the fwhm [$B_c = (B_{\text{obs}}^2 - B_{\text{inst}}^2)^{1/2}$, where B_{obs} is the observed peak width at the fwhm and B_{inst} is the instrumental peak broadening], and θ is the Bragg angle. See Cullity, B. D. *Elements of X-ray Diffraction*; Addison-Wesley: Reading, MA, 1978. Klug, H. P.; Alexander, L. E. *X-Ray Diffraction Procedures for Polycrystalline and Amorphous Materials*; Wiley: New York, 1974.

(22) The sizes of HFPD nanocrystals were estimated from the Scherrer equation, using the fwhm for the (010) reflection (after baseline correction and fitting to a Gaussian form). This analysis revealed that the fwhm of the nanocrystals was always greater than that of the bulk crystals, as anticipated. The crystal sizes never exceeded the channel diameter, with the crystals grown in the larger channels appearing to be much smaller

than the channel dimensions (crystal size = 16, 17, and 23 nm for 23-, 32-, and 40-nm p-PS and 17, 21, and 37 nm for 7.5-, 23-, and 55-nm CPG, respectively). This apparent discrepancy is likely due to the increased difficulty in measuring the fwhm accurately because the breadth of the peak approaches the instrument limit as the crystal size is increased. The sizes of the R-MAA nanocrystals were estimated from the fwhm of the diffraction peak at $2\theta = 20.2^\circ$. The reliability of these measurements, however, is questionable because the single-crystal structure is unknown and the existence of multiple (hkl) reflections under this diffraction peak, which would affect the fwhm, cannot be excluded.

(23) According to the manufacturer's specifications at least 80% of the pore volume lies within 10% of the nominal pore size. The remaining 20% of the pore volume is unspecified.

(24) Scherer, G. W. *Cem. Concr. Res.* **1999**, 29, 1347–1358.

(25) We note that the contact angles of molten HPFD on the glass and PS were 30 and 51° , respectively. The contact angles of molten R-MAA on the glass and PS were 14 and 40° , respectively. These values suggest that the specific surface energy of the melt-substrate interface, $\gamma_{\text{melt-sub}}$, is smaller on glass surfaces than on PS surfaces, which in turn suggests that the slopes in Figure 6 for CPG should be larger than those for PS, contrary to the observation. This apparent discrepancy most likely reflects the unique environment of the ultras-small channels, in which the walls are predominantly in contact with either the solid phase or the melt, with little free surface in contact with air. Consequently, deductions based on simple contact angle measurements, in which the substrate surface is in contact with air and may dominate the wetting characteristics, may be not valid. This argues that the model in Scheme 2 may indeed be a reasonable one.

(26) Sands, B. W.; Kim, Y. S.; Bass, J. L. *J. Chromatogr.* **1986**, 360, 353–369.